Science Advances

AAAS

advances.sciencemag.org/cgi/content/full/3/9/e1701010/DC1

Supplementary Materials for

Artificial solid electrolyte interphase for aqueous lithium energy storage systems

Jian Zhi, Alireza Zehtab Yazdi, Gayathri Valappil, Jessica Haime, P. Chen

Published 8 September 2017, *Sci. Adv.* **3**, e1701010 (2017)
DOI: 10.1126/sciadv.1701010

This PDF file includes:

- fig. S1. Characterizations of graphite, GO, and RGO.
- fig. S2. XRD patterns of the Blank cathode treated with hydrazine.
- fig. S3. Contact angle measurement results of the hydrazine aqueous solution on the GO-coated and Blank cathodes.
- fig. S4. SEM image of the 10RGO cathode obtained by 10 times layer-by-layer deposition of 1RGO.
- fig. S5. Rate capability results of the battery with the 10GO cathode (without hydrazine reduction) in comparison with the Blank cathode.
- fig. S6. Typical charge-discharge curves of ReHAB with the 10RGO cathode at 0.2 C.
- fig. S7. Capacity loss after 1-day float charge of the cathodes with different thicknesses of the G-SEI (1RGO, 5RGO, and 10RGO) and Blank cathodes (dip-coating GO and in situ reduction to RGO).
- fig. S8. Capacity loss after 1-day float charge of the 1RGO, 5RGO, 10RGO, and Blank cathodes (directly dip-coating RGO).
- fig. S9. Rate capability results of the pristine LMO and RGO-coated LMO particles in the cathode.
- fig. S10. Capacity loss after 1-day float charge and rate capabilities of Blank and 10RGO (thermally reduced) cathodes.
- fig. S11. The inside and outside of a large-scale battery cell (7 mA·hour) with 9-cm^2 cathode surface area for potential applications in the UPS power sources.
- fig. S12. Capacity loss after 1-day float charge of the 1RGO, 5RGO, 10RGO, and Blank cathodes in the large-scale cell (fig. S10) (mass loading of active materials, 25 to 28 mg cm^{-2}; L-S method to coat GO followed by water vapor reduction).

- fig. S13. Typical charge-discharge curves of the 10RGO-LMO/AC asymmetrical supercapacitor at different current densities.
- fig. S14. Cycling stability of the 10RGO-LMO/AC asymmetrical supercapacitor at a current density of 4 A g^{-1}.
- fig. S15. Relevant equivalent circuit model for EIS data in Fig. 3.
- fig. S16. R_{ct} of the 10RGO and Blank cathodes as a function of time without repeated cycles.
- fig. S17. R_s of the 10RGO and Blank cathodes as a function of repeated cycles of charge-discharge.
- fig. S18. R_s of the 10RGO and Blank cathodes as a function of time without repeated cycles.
- fig. S19. O1s peaks of the 10RGO cathode after the cycling test on the surface (red) and inside the bulk (blue).
- fig. S20. Coulombic efficiencies of the 10RGO and Blank samples during 300 cycles at 4 C.
- fig. S21. In situ XRD patterns of Blank and 10RGO cathode during discharge process ($Li_xMn_2O_4$, $0.11 < x < 1$).
- fig. S22. Contact angle results of the aqueous electrolytes on the Blank (left) and 10RGO (right) cathodes.
- fig. S23. The cycling properties of the Blank and 10RGO cathodes that are made of inactive silica particles rather than the LMO.
- fig. S24. Discharge curves of the 10RGO/silica cathode at a current density of 16 mA g^{-1}.
- fig. S25. Typical CVs of the 10RGO cathode at a scan rate of 0.1 to 0.7 mV s^{-1}.
- fig. S26. The peak current (i_p) in the 10RGO cathode samples (peak 1 in this study) as a function of the square root of the scan rate (v).
- Calculations of Li^+ diffusivity based on EIS data
- Calculations of Li^+ diffusivity based on CV plot
- Reference (*90*)

Supplementary Materials

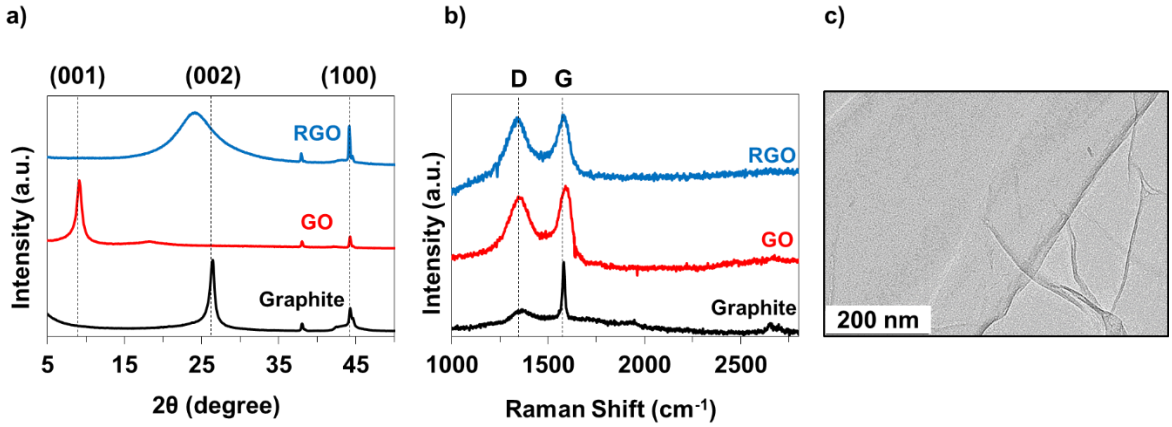

fig. S1. Characterizations of graphite, GO, and RGO. (**a**) XRD and (**b**) Raman of the starting graphite, the GO and the RGO powder samples. (**c**) HRTEM image of a wrinkled GO monolayer

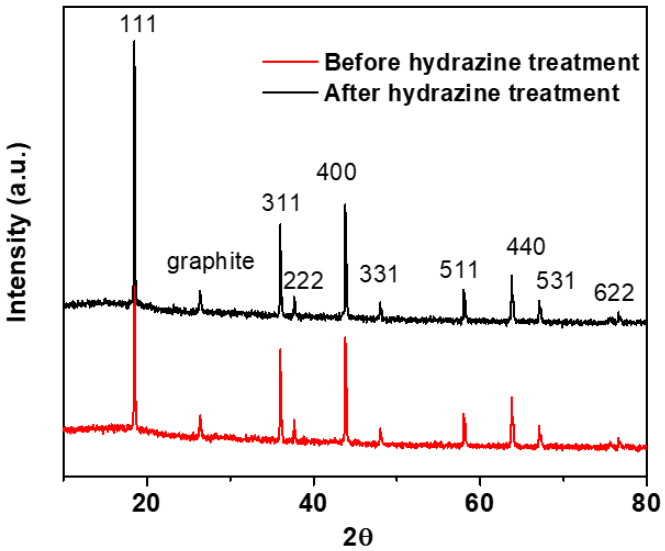

fig. S2. XRD patterns of the Blank cathode treated with hydrazine.

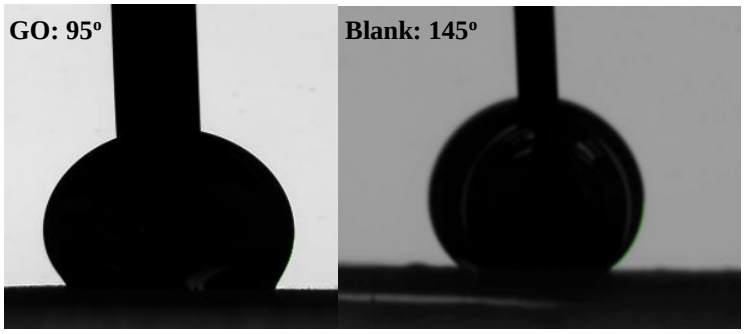

fig. S3. Contact angle measurement results of the hydrazine aqueous solution on the GO-coated and Blank cathodes.

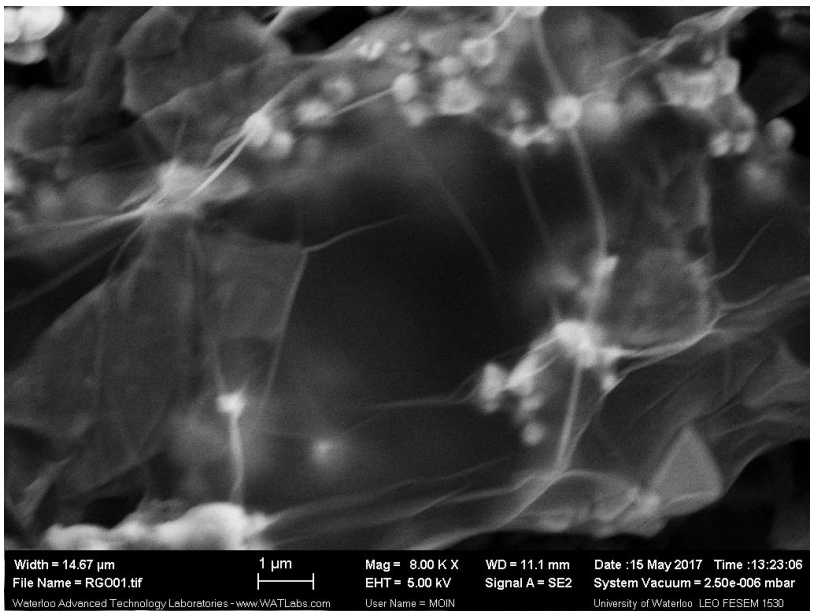

fig. S4. SEM image of the 10RGO cathode obtained by 10 times layer-by-layer deposition of 1RGO.

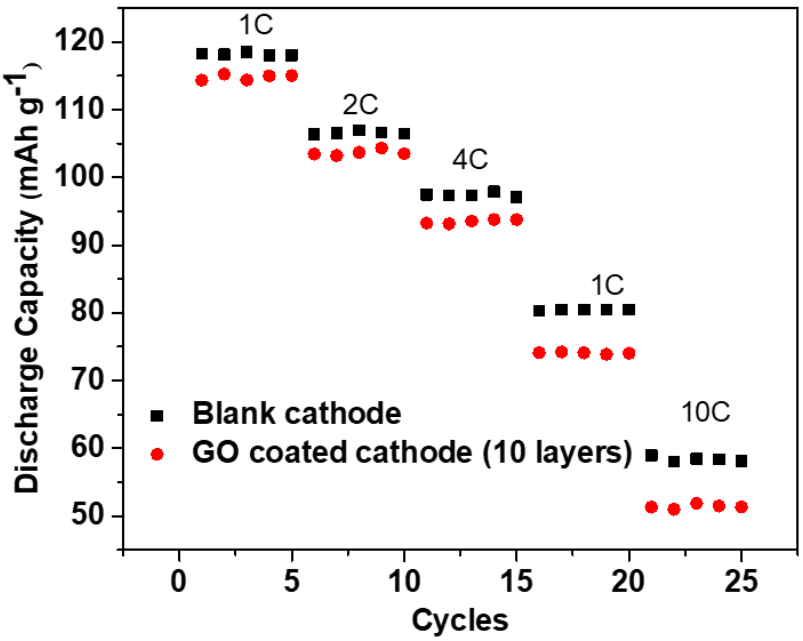

fig. S5. Rate capability results of the battery with the 10GO cathode (without hydrazine reduction) in comparison with the Blank cathode.

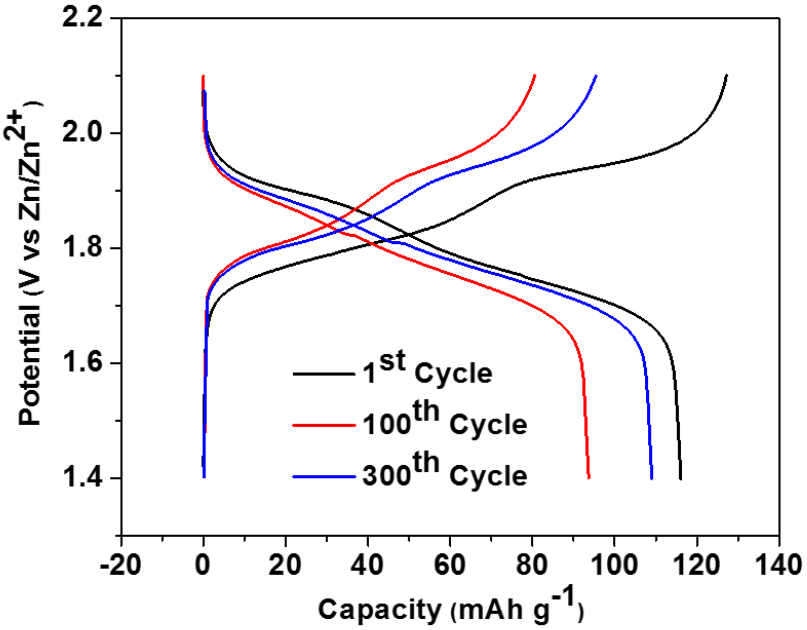

fig. S6. Typical charge-discharge curves of ReHAB with the 10RGO cathode at 0.2 C.

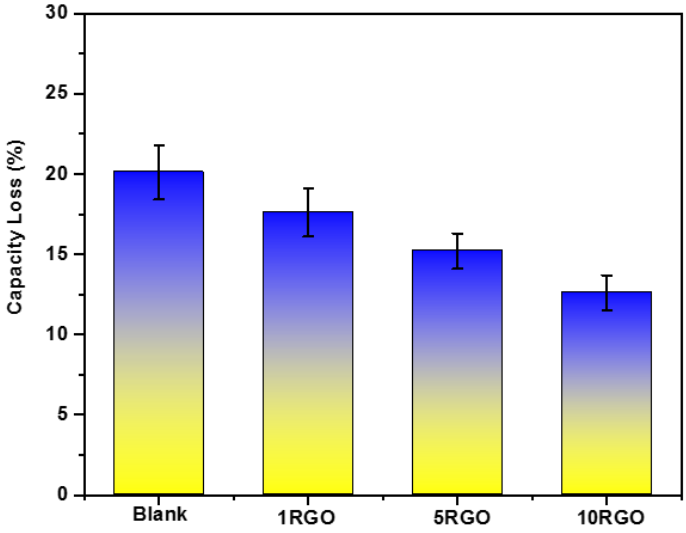

fig. S7. Capacity loss after 1-day float charge of the cathodes with different thicknesses of the G-SEI (1RGO, 5RGO, and 10RGO) and Blank cathodes (dip-coating GO and in situ reduction to RGO).

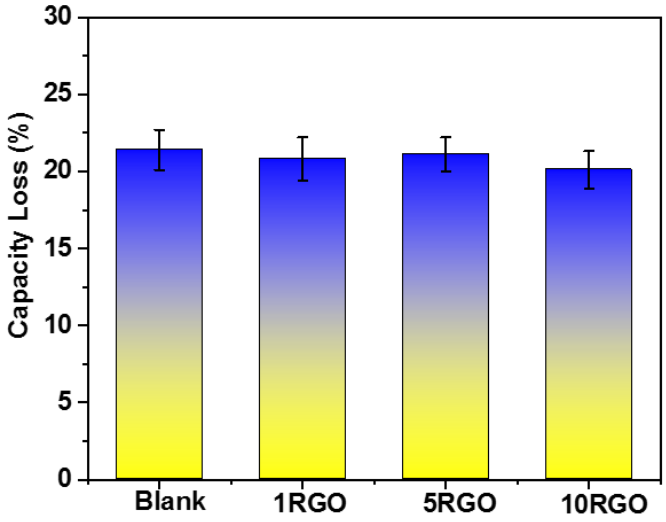

fig. S8. Capacity loss after 1-day float charge of the 1RGO, 5RGO, 10RGO, and Blank cathodes (directly dip-coating RGO).

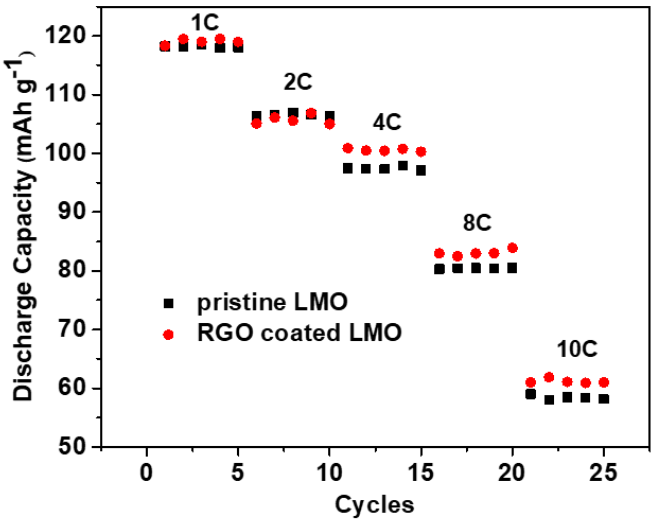

fig. S9. Rate capability results of the pristine LMO and RGO-coated LMO particles in the cathode.

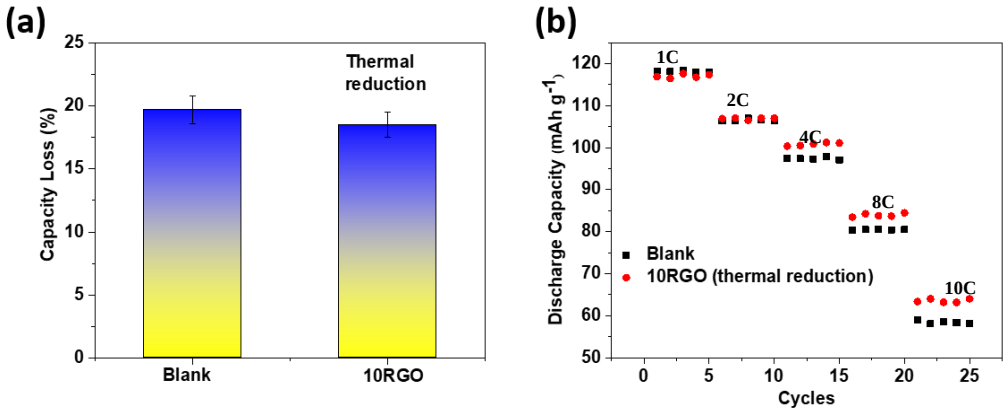

fig. S10. Capacity loss after 1-day float charge and rate capabilities of Blank and 10RGO (thermally reduced) cathodes. (**a**) Capacity loss after 1day float charge and (**b**) rate capabilities of Blank and 10RGO (thermally reduced) cathodes.

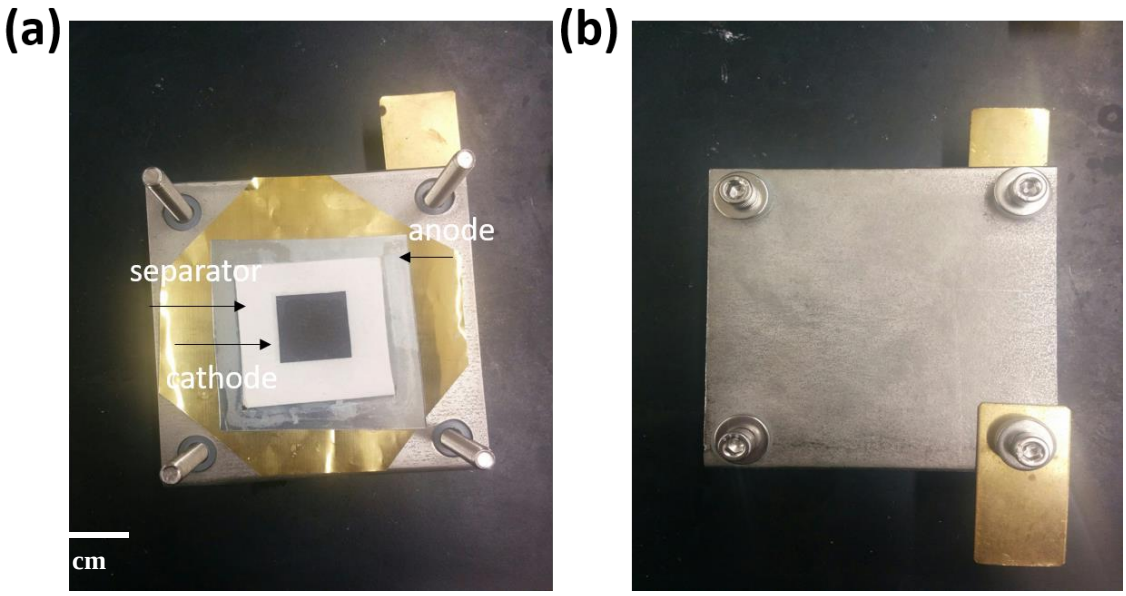

fig. S11. The inside and outside of a large-scale battery cell (7 mA·hour) with 9-cm^2 cathode surface area for potential applications in the UPS power sources. (a) The inside, and (**b**) the outside of a large-scale battery cell (7 mAh) with 9 cm^2 cathode surface area for potential applications in the UPS power sources.

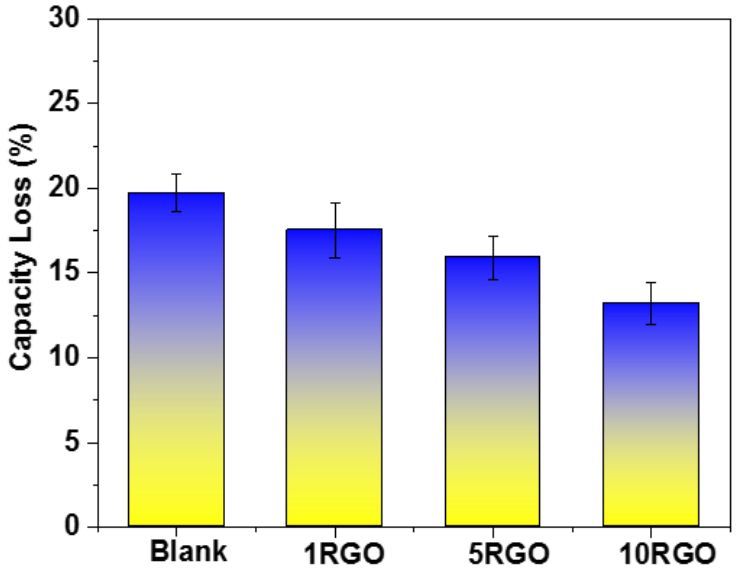

fig. S12. Capacity loss after 1-day float charge of the 1RGO, 5RGO, 10RGO, and Blank cathodes in the large-scale cell (fig. S10) (mass loading of active materials, 25 to 28 mg cm^{-2}; L-S method to coat GO followed by water vapor reduction).

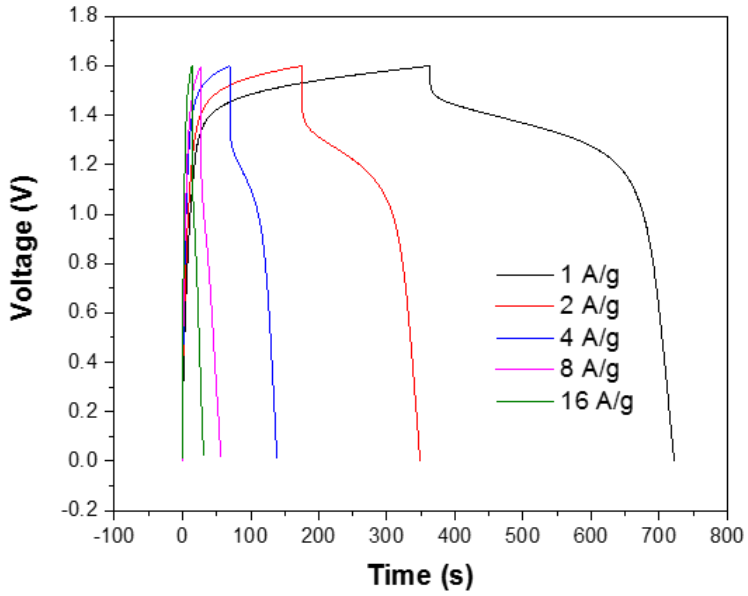

fig. S13. Typical charge-discharge curves of the 10RGO-LMO/AC asymmetrical supercapacitor at different current densities.

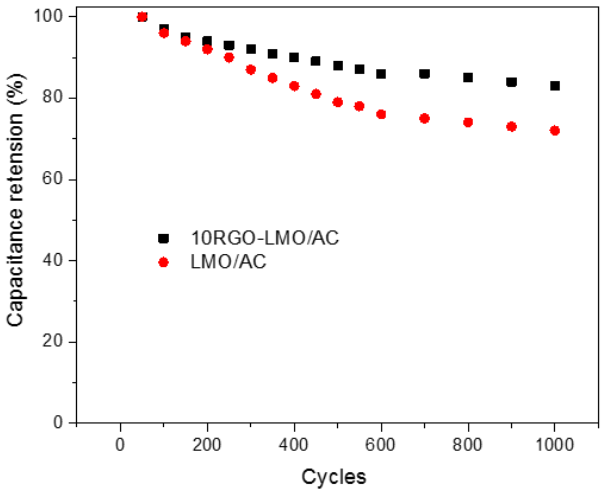

fig. S14. Cycling stability of the 10RGO-LMO/AC asymmetrical supercapacitor at a current density of 4 A g^{-1}.

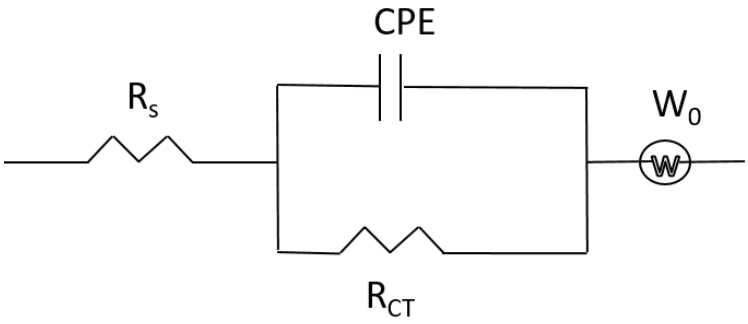

fig. S15. Relevant equivalent circuit model for EIS data in Fig. 3.

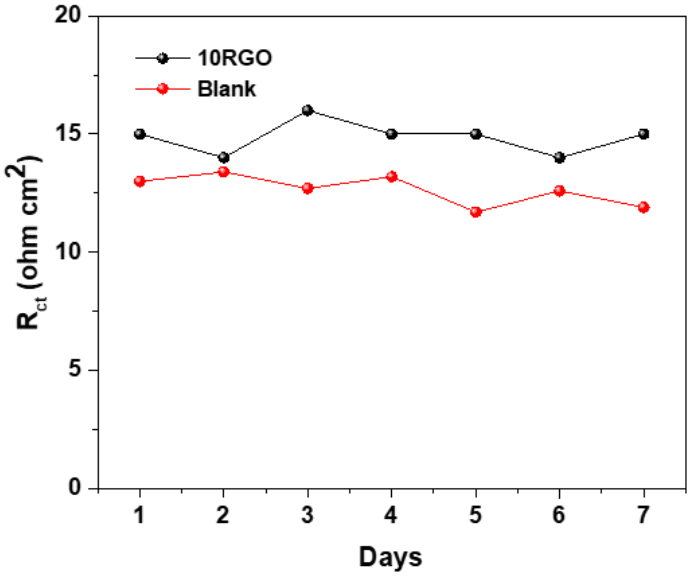

fig. S16. R_{ct} of the 10RGO and Blank cathodes as a function of time without repeated cycles.

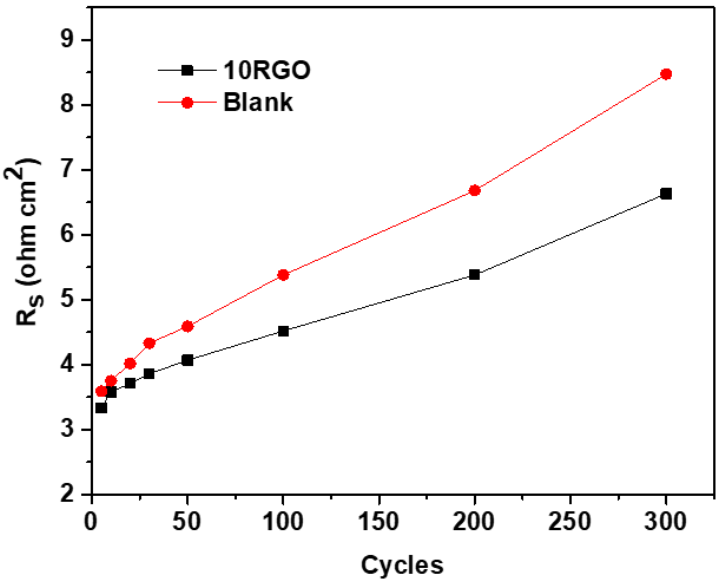

fig. S17. R_s of the 10RGO and Blank cathodes as a function of repeated cycles of charge-discharge.

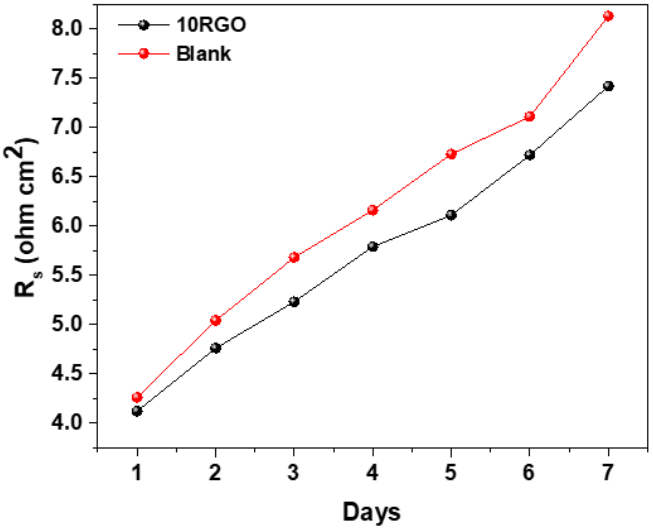

fig. S18. R_s of the 10RGO and Blank cathodes as a function of time without repeated cycles.

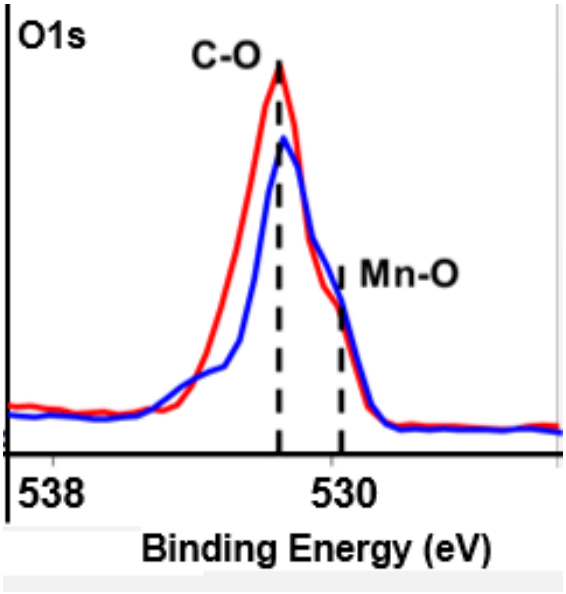

fig. S19. O1s peaks of the 10RGO cathode after the cycling test on the surface (red) and inside the bulk (blue).

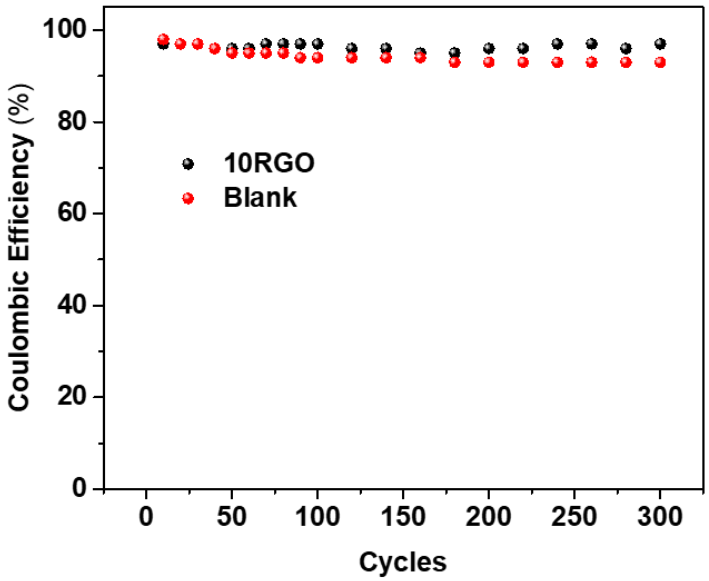

fig. S20. Coulombic efficiencies of the 10RGO and Blank samples during 300 cycles at 4 C.

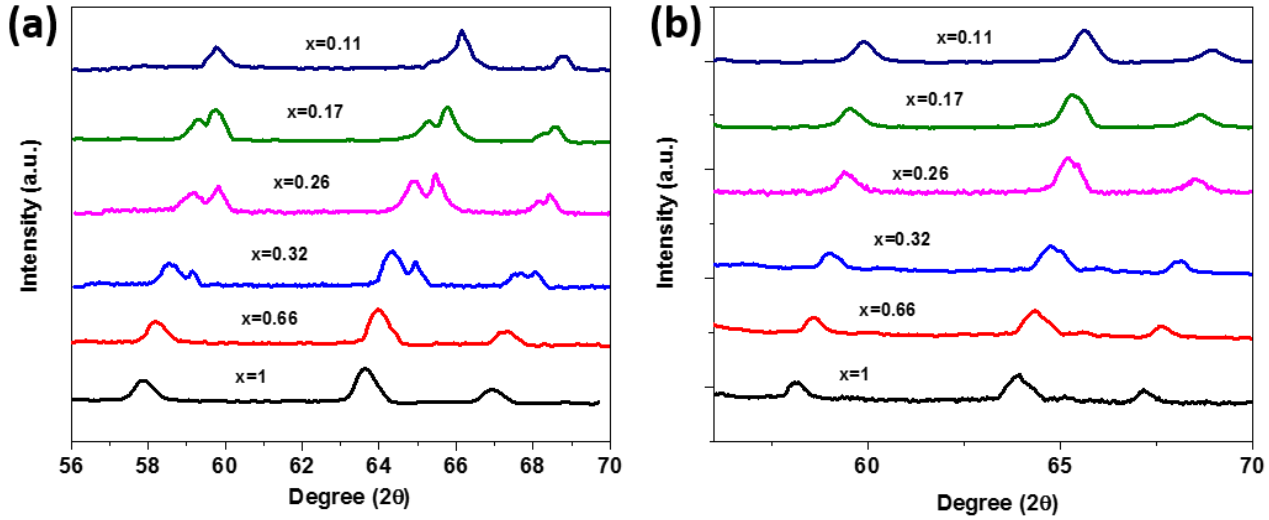

fig. S21. In situ XRD patterns of Blank and 10RGO cathode during discharge process ($Li_xMn_2O_4$, 0.11 < *x* < 1). In situ XRD patterns of (**a**) Blank and (**b**) 10RGO cathode during discharge process ($Li_xMn_2O_4$, 0.11<x<1).

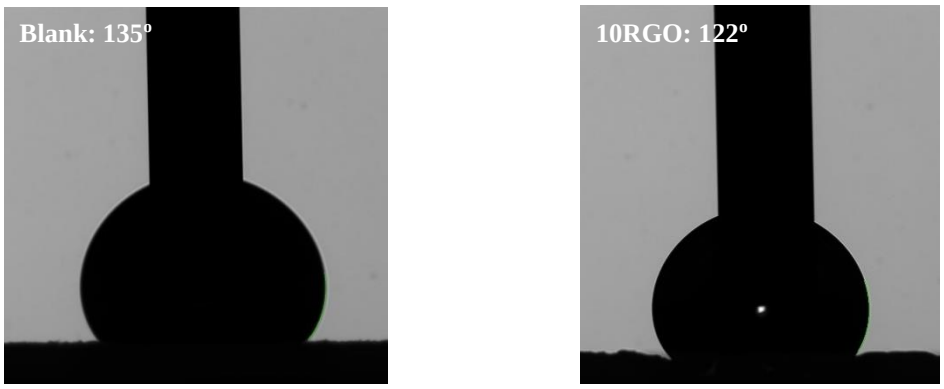

fig. S22. Contact angle results of the aqueous electrolytes on the Blank (left) and 10RGO (right) cathodes.

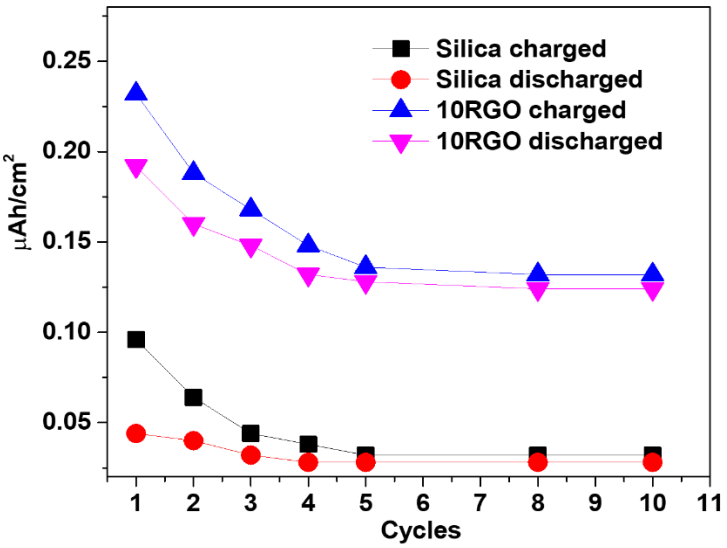

fig. S23. The cycling properties of the Blank and 10RGO cathodes that are made of inactive silica particles rather than the LMO.

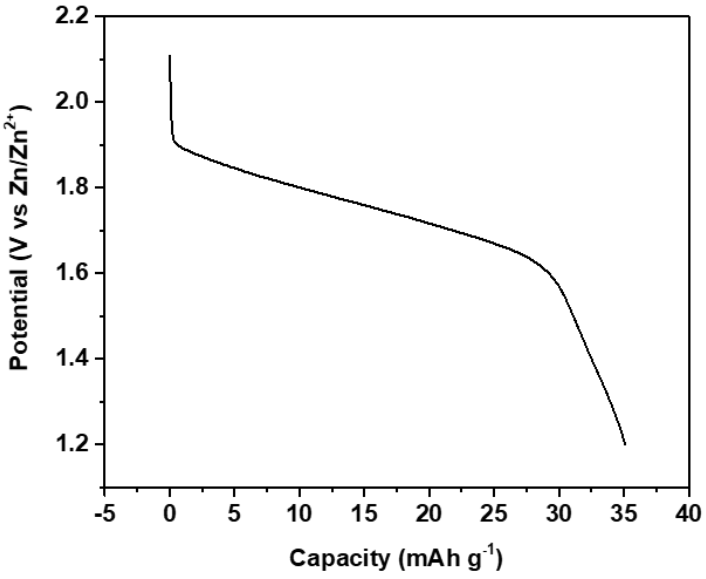

fig. S24. Discharge curves of the 10RGO/silica cathode at a current density of 16 mA g^{-1}.

Calculations of Li^+ diffusivity based on EIS data

EIS results are fitted using an equivalent circuit. In the equivalent circuit, R_s indicates the ohmic resistance of electrolyte and electrode; R_{ct} is attributed to the charge-transfer resistance at the active material interface; CPE represents the double-layer capacitance and passivation film capacitance. W is the Warburg impedance caused by a semi-infinite diffusion of Li^+ ion in the electrode. Z_{re} from EIS is highly related to the root square of the lower angular frequencies. Through linear fitting, the Warburg impedance coefficient (σ_w) can be obtained from the straight lines. The relation is governed by Eq. (1)

$$Z_{re} = R_s + R_{ct} + \sigma_w \omega - 1/2 \quad (1)$$

where R_{ct}: charge-transfer resistance, Rs: ohmic resistance and ω: angular frequency in the low frequency region. After obtaining σ_w, the diffusivity values of the lithium ions diffusing into the electrode materials can be further calculated using Eq. (2)

$$D_{Li} = 0.5 \left(\frac{RT}{AF^2 \sigma_w C}\right)^2 \quad (2)$$

D_{Li}: Li^+ diffusivity, R: the gas constant, T: the absolute temperature, F: Faraday's constant, A: the contact area between active materials and electrolyte (here the geometric area of electrode) and C: molar concentration of Li^+ ions.

Calculations of Li^+ diffusivity based on CV plot

To evaluate the electrode kinetics of the RGO coated cathodes, the Li^+ diffusivity (diffusion coefficient) was determined from the results of CV at various scan rates over the potential range of 1.4-2.1 V at room temperature by the Randles-Sevick equation. In the typical CVs of the RGO-coated cathodes at scan rate of 0.1-0.7 mVs^{-1} (10RGO, fig. S24), the anodic and the cathodic peaks were assigned to 1,2 and 1',2', respectively. As plotted in fig. S25, the peak current (i_p) in 10RGO, 5RGO, 1RGO and blank cathode samples (peak 1 in this study) was highly related to the square root of the scan rate (v) during the de-intercalation and intercalation of Li^+, thus the electrochemical reaction rate would be controlled by a semi-infinite diffusion process (*90*). The diffusivity of the Li^+ (D_{Li}) at room temperature (25 °C) can be calculated from Equation (1) as follows

$$i_p = 2.69\times10^5 n^{2/3} A D_{Li}^{1/2} v^{1/2} C_0 \quad (1)$$

where i_p is the peak current (A), n is the number of electrons per reaction species, A is the apparent area of the electrode (cm^2), D_{Li} is the diffusivity of Li^+ ($cm^2\ s^{-1}$), C_0 is the bulk concentration of Li^+ in $LiMn_2O_4$ (0.02378 mol cm^{-3} derived from the theoretical density of 4.3 g cm^{-3}), and v is the sweep rate (Vs^{-1}) (*53*). Accordingly, from the slope of each linear fit, D_{Li} based on peak 1 was calculated to be 6.19×10^{-9} cm^2s^{-1} for the 10RGO samples before cycling test. D_{Li} values of 10RGO after cycling test, as well as D_{Li} of Blank before and after cycling test have been also calculated by the same method.

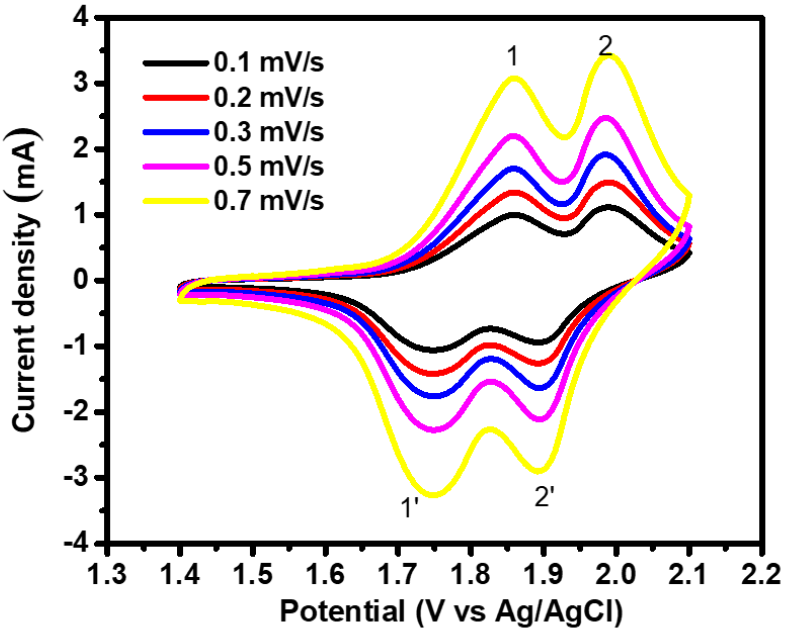

fig. S25. Typical CVs of the 10RGO cathode at a scan rate of 0.1 to 0.7 mV s^{-1}.

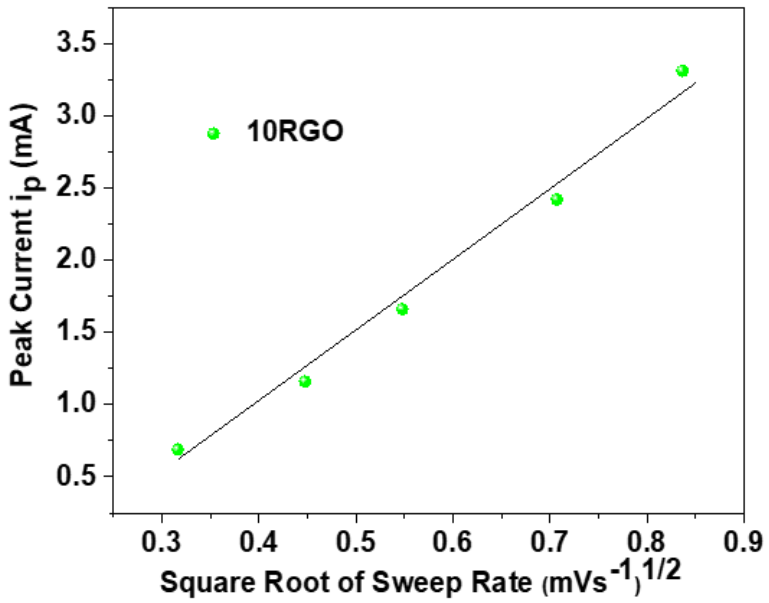

fig. S26. The peak current (i_p) in the 10RGO cathode samples (peak 1 in this study) as a function of the square root of the scan rate (v).